

## Effect of fluid topology on residual nonwetting phase trapping: Implications for geologic CO<sub>2</sub> sequestration



Anna L. Herring<sup>a,\*</sup>, Elizabeth J. Harper<sup>a</sup>, Linnéa Andersson<sup>a</sup>, Adrian Sheppard<sup>b</sup>, Brian K. Bay<sup>c</sup>, Dorte Wildenschild<sup>a</sup>

<sup>a</sup>School of Chemical, Biological and Environmental Engineering, Oregon State University, Corvallis, OR 97331, USA

<sup>b</sup>Research School of Physics and Engineering, Australian National University, Canberra, ACT 0200, Australia

<sup>c</sup>School of Mechanical, Industrial, and Manufacturing Engineering, Oregon State University, Corvallis, OR 97331, USA

### ARTICLE INFO

#### Article history:

Received 15 May 2013

Received in revised form 25 September 2013

Accepted 27 September 2013

Available online 7 October 2013

#### Keywords:

Connectivity

Topology

CO<sub>2</sub> sequestration

Capillary trapping

Porous media

X-ray tomography

### ABSTRACT

This work examines the influence of *initial* (i.e. post drainage) nonwetting (NW) fluid topology on total *residual* (i.e. after imbibition) NW phase saturation. Brine and air (used as a proxy for supercritical CO<sub>2</sub>) flow experiments were performed on Bentheimer sandstone; results were quantified via imaging with X-ray computed microtomography (X-ray CMT), which allows for three dimensional, non-destructive, pore-scale analysis of the amount, distribution, and connectivity of NW phase fluid within the sandstone cores. In order to investigate the phenomenon of fluid connectivity and how it changes throughout flow processes, the Bentheimer sandstone results are compared to previously collected X-ray CMT data from similar experiments performed in a sintered glass bead column, a loose packed glass bead column, and a column packed with crushed tuff. This allows us to interpret the results in a broader sense from the work, and draw conclusions of a more general nature because they are not based on a single pore geometry. Connectivity is quantified via the *normalized Euler number* of the NW fluid phase; the Euler number of a particular sample is normalized by the maximum connectivity of the media, i.e. the Euler number of the system at 100% NW phase saturation. General connectivity-saturation relationships were identified for the various media. In terms of trapping, it was found that residual NW phase trapping is dependent on initial (i.e. post-drainage) NW phase connectivity as well as imbibition capillary number for the Bentheimer sandstone. Conversely, the sintered glass bead column exhibited no significant relationship between trapping and NW topology.

These findings imply that for a CO<sub>2</sub> sequestration scenario, capillary trapping is controlled by both the imbibition capillary number and the initial NW phase connectivity: as capillary number increases, and the normalized initial Euler number approaches a value of 1.0, capillary trapping is suppressed. This finding is significant to CO<sub>2</sub> sequestration, because both the drainage (CO<sub>2</sub> injection) and imbibition (subsequent water injection or infiltration) processes can be engineered in order to maximize residual trapping within the porous medium. Based on the findings presented here, we suggest that both the Euler number-saturation and the capillary number-saturation relationships for a given medium should be considered when designing a CO<sub>2</sub> sequestration scenario.

© 2013 Elsevier Ltd. All rights reserved.

### 1. Introduction

Energy production via the use of fossil fuels has resulted in the release and accumulation of substantial quantities of CO<sub>2</sub> in the atmosphere [1]. The prevalence and amount of coal in reserves throughout the world implies that despite concerns of excessive anthropogenic CO<sub>2</sub> emissions, coal will continue to be a large source of energy production in the future; this indicates that some form of emissions mitigation is necessary for coal-based power plants or other concentrated emission sources [2]. Geologic

sequestration of CO<sub>2</sub> has been suggested as a mitigation strategy with regards to energy production via coal power plants [3], and both short and long term security of storage of CO<sub>2</sub> in the subsurface is essential to a successful sequestration scheme.

Sequestration involves (1) injection of supercritical CO<sub>2</sub> into a subsurface brine reservoir, considered to be a brine drainage process; and (2) the subsequent upward travel of the buoyant CO<sub>2</sub> plume, during which the brine passively imbibe or is injected into the pore space. Ultimately, the CO<sub>2</sub> may dissolve into the brine (“dissolution trapping”) and eventually precipitate to form carbonate minerals (“mineral trapping”). However, these dissolution and precipitation processes are estimated to occur on long timescales (on the order of hundreds to thousands of years) and a mobile

\* Corresponding author. Tel.: +1 9706293174.

E-mail address: [herring@engr.orst.edu](mailto:herring@engr.orst.edu) (A.L. Herring).

CO<sub>2</sub> plume may exist in the subsurface until these reactions proceed to completion [3]. Entrapment of CO<sub>2</sub> via capillary forces within the pore structure of the rock (“capillary trapping”) occurs on short time scales, and is more secure than trapping of a continuous CO<sub>2</sub> plume via a caprock (“hydrodynamic trapping” or “structural trapping”) [3].

In theory, maximization of capillary trapping can be accomplished via manipulation of injection scenarios. Parameters such as pressure, temperature, and salinity conditions of the injection can be sought such that the fluid properties and thus interaction of the CO<sub>2</sub>-brine system are most conducive to capillary trapping. Similarly, the flow rates and volumes of both the CO<sub>2</sub> injection and the subsequent brine injection/imbibition can be managed to provide favorable capillary trapping conditions.

This approach is similar to that of enhanced oil recovery wherein different fluid and flow properties are manipulated in order to extract the maximum amount of oil from a subsurface reservoir; and indeed, much of the prior research in the area of CO<sub>2</sub> sequestration is adapted from traditional oil recovery research. However, the CO<sub>2</sub> sequestration process differs from oil recovery in two significant aspects: (1) the goal of a sequestration scheme is to trap, rather than mobilize, the greatest amount of nonwetting fluid possible; and (2) during a sequestration scenario the drainage (and thus, the *initial* state) of the reservoir can be engineered as well as the imbibition (the *residual* state); while in oil extraction operations only the imbibition process can be varied, as the initial state of the reservoir is predetermined by the reservoir itself. Therefore, in order to design a successful CO<sub>2</sub> sequestration scheme, maximization of capillary trapping of supercritical CO<sub>2</sub> via manipulation of both the drainage and imbibition processes must be investigated. In this work, we use the standard nomenclature of drainage (i.e. NW phase invading pore space and displacing W phase) and imbibition (W phase invading pore space and displacing NW phase); but to emphasize the importance of NW fluid in a CO<sub>2</sub> sequestration scenario, all saturation values are presented as NW saturation.

It is generally accepted that the absolute amount of capillary trapped NW phase (i.e. the residual NW phase saturation) for a given medium is related to the Capillary Number (Ca) of the imbibition, or water flooding, process. Ca has several definitions depending on the intended application [4,5], but has traditionally been defined from an oil extraction standpoint. In general, the capillary number describes the balance between viscous forces and capillary forces with respect to the invading fluid (as opposed to the defending fluid). In this work, Ca is defined as:

$$Ca = \mu_{INV} v_{INV} / \sigma$$

where  $v_{INV} = Q / (A \cdot \eta)$

Here, viscous forces are represented by the product of the invading phase viscosity [mPa s] and the invading phase velocity [m/s]. Capillary forces are represented by the interfacial tension between the two fluid phases [mN/m]. The invading phase velocity is calculated as the volumetric flow rate  $Q$  [m<sup>3</sup>/s] divided by the cross-sectional area  $A$  [m<sup>2</sup>] of the porous medium and the porosity  $\eta$  [-].

For an imbibition process, the amount of trapped NW phase (i.e. residual NW phase normalized by initial NW phase) will be high at lower Ca values, but will decrease sharply if the imbibition process exceeds some threshold or “critical” capillary number (e.g. [6]); this is due to the transition from capillary to viscous force dominance. This relationship has been demonstrated extensively with experimental work [7–9], as well as numerical modeling [10,11]. NW trapping is not purely a function of Ca, however, as this relationship will shift in response to changes in NW fluid [12] or medium properties [11]. Another factor influencing residual saturation is the initial saturation of NW fluid in the medium prior

to imbibition [13,14]: residual NW saturation increases as initial NW saturation increases. This general trend is shown to hold for many media types, although there is still variation among different media types (Fig. 1, from [13]).

In order to quantify the differences in fluid transport in different media, topological and morphological measures have been utilized to characterize the internal structure of porous media and relevant media properties for fluid flow [15–20]. Additional work has been done to try to identify specific geometric properties of media which lead to increased NW residual trapping. For example, Chatzis et al. [21] looked at several different experimental systems (glass bead packs, two-dimensional (2D) micromodels, and Berea sandstone) and two trapping mechanisms: snap-off (where a NW fluid blob is trapped in a pore while W fluid flows around and through that same pore) vs. bypassing (where a NW filled pore remains filled while W fluid flows through an adjacent pore). Chatzis et al. [21] concluded that residual NW phase distribution and trapping type is dependent on the pore-throat aspect ratio (the ratio of the pore body radius to the throat radius) with secondary consideration given to the coordination number (the number of throats associated with a single pore). In support of this conclusion, Al-Raoush and Willson [22] utilized X-ray tomography to identify residual NW phase within a glass bead pack and found that NW phase was trapped primarily in the pore bodies with the highest aspect ratio and highest coordination number.

However, unlike previous work that has concentrated on the shape and structure of the porous media itself, there are relatively few works that study the topology of the NW fluid phase within a porous medium. In one of the few studies to address this topic, Wardlaw and Yu [23] used 2D micromodels to investigate NW phase topology and found that a more highly connected initial NW phase leads to a decrease in residual saturation. Further, Wardlaw and Yu [23] also state that the effect of NW phase topology is more important for media with low pore-throat aspect ratio, and uniform pore size distributions.

Wardlaw and Yu’s work [23] suggests that in addition to the Ca dependent trapping and initial-residual effects discussed above, residual NW phase trapping can be maximized by manipulating CO<sub>2</sub> injection to produce desirable initial state NW phase connectivity. Additionally, the relative importance of fluid topology for different media implies that different injection schemes (e.g. water alternating gas, or WAG) resulting in different fluid topologies may have varying efficiencies for different media. In order to examine these theories, the following research questions are addressed in this work:

- How is NW phase connected in different porous media after drainage and after imbibition?

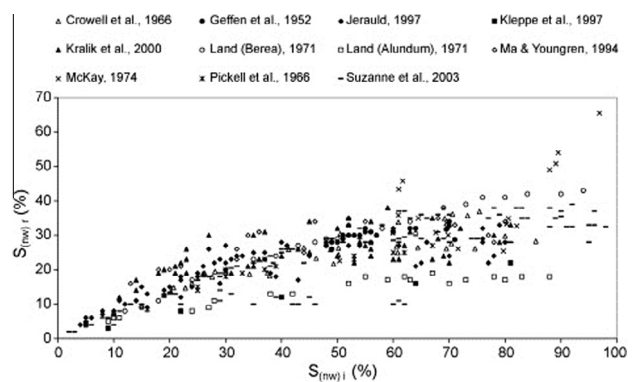


Fig. 1. Literature values for residual nonwetting (NW) saturation  $S_{(nw)r}$  as a function of initial non-wetting saturation  $S_{(nw)i}$  [13].

- How does initial state NW fluid topology affect residual NW fluid trapping?
- How does fluid topology affect trapping in different media?
- How can initial NW phase fluid topology be controlled to optimize residual trapping?

In addition, this work will verify the effect of imbibition capillary number on capillary trapping in Bentheimer sandstone. This research aims to investigate these questions on a quantitative, pore-scale basis via the use of X-ray computed microtomography (X-ray CMT). X-ray CMT is a non-destructive method of sample analysis which has been utilized in geology, hydrology, and oil recovery work in order to visualize and characterize the internal three-dimensional (3D) structure of porous media [22,24–29]. For a thorough overview of the use of X-ray CMT in fluid flow experiments, the reader is referred to Wildenschild and Sheppard [30].

To our knowledge, this is the first research studying the 3D topology of a *fluid phase* within a porous medium (in contrast to recent work by Vogel [17], Lehmann et al. [31], and Hilpert et al. [32] which focused on the topological characteristics of the porous medium). We present topological characterization (via the use of the Euler Number,  $\chi$ , described further in the Theory section) of a nonwetting fluid, air ( $\text{CO}_2$  proxy), after NW phase trapping experiments in 6 mm diameter Bentheimer sandstone and sintered glass bead cores. To further investigate NW phase connectivity behavior in porous media, additional topological analysis is performed on previously collected data from brine and air drainage-imbibition scanning curve experiments in a loosely packed glass bead core and crushed tuff column.

The W phase used in these experiments, 1:6 by mass potassium iodide brine, approximates the W phase for a  $\text{CO}_2$  geologic sequestration operation; and in addition the iodine acts as a contrast agent for CMT scanning. The  $\text{CO}_2$  proxy fluid, air, is chosen to facilitate ease of experiments and thus provide a large amount of experimental data. The air-brine-Bentheimer system approximates the combination of capillary, viscosity, and gravity forces which control a supercritical  $\text{CO}_2$ -brine-sandstone system (e.g. [33]). While these experiments cannot be said to be directly representative of the supercritical  $\text{CO}_2$ -brine system, both systems should show the same general response to flow processes on a pore-scale basis; this implies that processes we observe in the ambient experimental Bentheimer system will be relevant to geologic sequestration of  $\text{CO}_2$ .

The remainder of this article will detail the materials and methods of our experiments and analysis; a brief introduction to topology and the Euler number; the results of our analysis, and discussion of the results. Finally, conclusions and application to  $\text{CO}_2$  sequestration scenarios will be addressed.

## 2. Material and methods

Four data sets are analyzed in this work. Two data sets arise from NW trapping experiments consisting of one drainage-imbibition cycle, conducted in Bentheimer sandstone cores (new

experimental data) and sintered glass bead packs [34]. The remaining two data sets arise from multiple drainage-imbibition cycles performed in loose granular packs, one of glass beads [35] and one of crushed tuff [36]. Relevant experimental parameters are shown in Table 1.

### 2.1. Bentheimer sandstone

Bentheimer sandstone was chosen as a model porous media for  $\text{CO}_2$  sequestration studies because (1) it is relevant to geologic formations which have been identified as potential sequestration sites; and (2) the pore and grain features are sized such that it is a suitable porous medium for analysis by X-ray CMT. The Bentheimer rock samples were cored from larger blocks of sandstone, which all originated from the same formation and are expected to have similar pore size distributions, permeabilities, porosities, and aspect ratios. All cores had a diameter of 6 mm; core lengths ranged from 28 to 45 mm. The cores were wrapped with a thin layer of Teflon tape and epoxied into aluminum core holders (Fig. 2b).

A Harvard PHD2000 syringe pump (Harvard Apparatus, Holliston MA, United States) was used to precisely control volumes and drainage and imbibition flow rates of fluids. A low-range and a high-range pressure transducer (Validyne Engineering, Northridge CA, United States) were connected in parallel to allow for verification of pressure measurements and allow for measurement of a wide range of pressure values. The low-range transducer provided fine pressure measurements at low pressure and was disconnected at higher pressures (i.e.  $\pm 13.7$  kPa or  $\pm 140$  cm  $\text{H}_2\text{O}$ ) to prevent failure of the pressure transducer membrane, at which point the high-range transducer was utilized. A schematic of the experimental set-up is shown in Fig. 2a.

#### 2.1.1. Experimental process

Prior to an experiment, the rock core was flushed with gaseous  $\text{CO}_2$  for 30 min at a pressure of approximately 100 kPa (15 psi) to attempt to replace all the air in pores with gaseous  $\text{CO}_2$ . Gaseous  $\text{CO}_2$  is more soluble than air; the  $\text{CO}_2$  (g) flushing increases the dissolution of the gas within gas-filled pores and results in a higher brine saturation at the initial stage of the flow experiment. Two layers of hydrophilic nylon membrane with 1.2  $\mu\text{m}$  pore size (General Electric Company, Fairfield CT, United States) were used at the base of the sample stage, thus preventing NW fluid from entering the brine line during the drainage process. The complete core holder assembly is shown in Fig. 2c. The  $\text{CO}_2$  (g)-filled rock core was attached to the sample base and flushed with 10 pore volumes of 1:6 by mass potassium iodide brine at a relatively high flow rate (1 mL/min, corresponding to  $\text{Ca} \approx 10^{-5}$ ); the system was then allowed to equilibrate for at least 30 min to enhance dissolution of the pore space  $\text{CO}_2$  (g), and then another 10 pore volumes of brine were pumped through to remove any acidified brine from the sandstone core.

After these preliminary steps, the drainage-imbibition experiment commenced; approximate W and NW saturations

**Table 1**  
Experimental parameters.

Medium	$d_{50}$ ( $\mu\text{m}$ )	Ca	Column length (mm)	Column I.D. (mm)	Image resolution ( $\mu\text{m}$ )
<i>NW trapping experiments</i>					
Bentheimer sandstone	190 <sup>a</sup>	$10^{-8.6}$ – $10^{-5.1}$	28–45	6	10
Sintered glass bead	850	$10^{-6.0}$ – $10^{-3.6}$	56	5.7	13
<i>Scanning curve experiments</i>					
Loose pack glass bead	850	$10^{-7.7}$ – $10^{-7.6}$	70	7.0	17
Crushed tuff	1795	$10^{-6.8}$ – $10^{-6.0}$	42	6	17.5

<sup>a</sup> From Maloney et al. [38].

throughout the experimental process and the analogy to the CO<sub>2</sub> sequestration process is shown in Fig. 3. At the beginning of the experiment, the sandstone system was assumed to represent a fully W fluid saturated state; however, there was still a small residual amount of gas after this process ( $\leq 6\%$  of the pore space). A scan of the core was acquired to record the *original* NW phase saturation ( $S_0$ ). Upon completion of the  $S_0$  scan, the core was drained at a low flow rate ( $0.3 \mu\text{l}/\text{min}$ ,  $Ca \approx 10^{-8.6}$ ) via retraction of the syringe pump to a specified volume resulting in initial NW saturation values ranging from 35% to 75%. Pressure was carefully monitored during this process to ensure there were no leaks or membrane failure. Upon completion of drainage, another scan was acquired of this NW phase *initial* saturation ( $S_1$ ). Finally, wetting fluid was re-imbibed into the core at various flow rates (i.e. 0.0003, 0.003, 0.03, 0.06, 0.3, or 0.9 ml/min) until brine appeared and covered the top of the core, and pressure was monitored here to ensure appropriate forced-imbibition response (i.e. a pressure spike until water breakthrough, followed by equilibrium pressure equivalent to the pressure drop across the core). A final scan was acquired of the core at this *residual* NW phase saturation ( $S_R$ ). The core was cleaned by flushing with approximately 100 pore volumes of deionized water and either vacuum or oven-dried.

### 2.1.2. X-ray CMT and image processing

The scanner used for these experiments was a CMT system housed in the School of Mechanical, Industrial, and Manufacturing Engineering at Oregon State University and utilizes a cone-beam MicroFocus FXE-160.20 X-ray source, and projections were collected with a  $2448 \times 2048$  pixel (16-bit) CCD camera (Point Grey Research, GRAS-50S5 M-C), coupled to an image intensifier (Medellex model HXS-93/PS). All scans were conducted at 110 kV and  $71 \mu\text{A}$ . Each scan consisted of  $360^\circ$  of rotation in 1400 increments

with 6 images averaged per increment, resulting in scan times of 2.25–3 h. Resolution for these scans was approximately  $10 \mu\text{m}$ .

The raw data consisted of a multitude of radiographs which were first corrected for spatial distortion with a grid-based algorithm, and normalized for beam intensity non-uniformity using light and dark image based flat-field correction. The individual radiographs were then reconstructed into a 3D volume using Octopus, a tomography reconstruction software (inCT, Ghent, Belgium).

The geometry of the pore bodies and throats in Bentheimer sandstone results in partial volume effects. Ring artifacts and general noise produced by the X-ray CMT system also contribute artifacts to the reconstructed volume. Thus, segmentation of this data requires a more sophisticated method than simple grayscale histogram segmentation. A subsection ( $550^3$  voxels) of the total volume was specified (generally containing the midpoint in the z-direction of the core) to be analyzed. This subvolume was segmented using 3DMA-Rock, which utilizes Indicator Kriging segmentation [37]. Due to the relatively high level of noise and low resolution of the Bentheimer data, only two phases were identified in these volumes: NW phase vs. combined solid/W phase.

3DMA-Rock implements Indicator Kriging on the three-dimensional (3D) data set by identifying all pixels in the image which are below a lower threshold or above an upper threshold and labeling them as NW phase or solid/W phase respectively. For all pixels with grayscale values between the two thresholds, kriging was used to determine which phase to classify the pixels as. This process is shown for a 2D slice in Fig. 4. Each scan had a different amount of wetting fluid present, resulting in a different average attenuation for the volume and thus a different post-reconstruction scaling of grayscale values, so it was not possible to use a single set of threshold values for all scans. Instead, each scan is run through the program using multiple thresholds sets and the threshold set which provided the most accurate labeling was

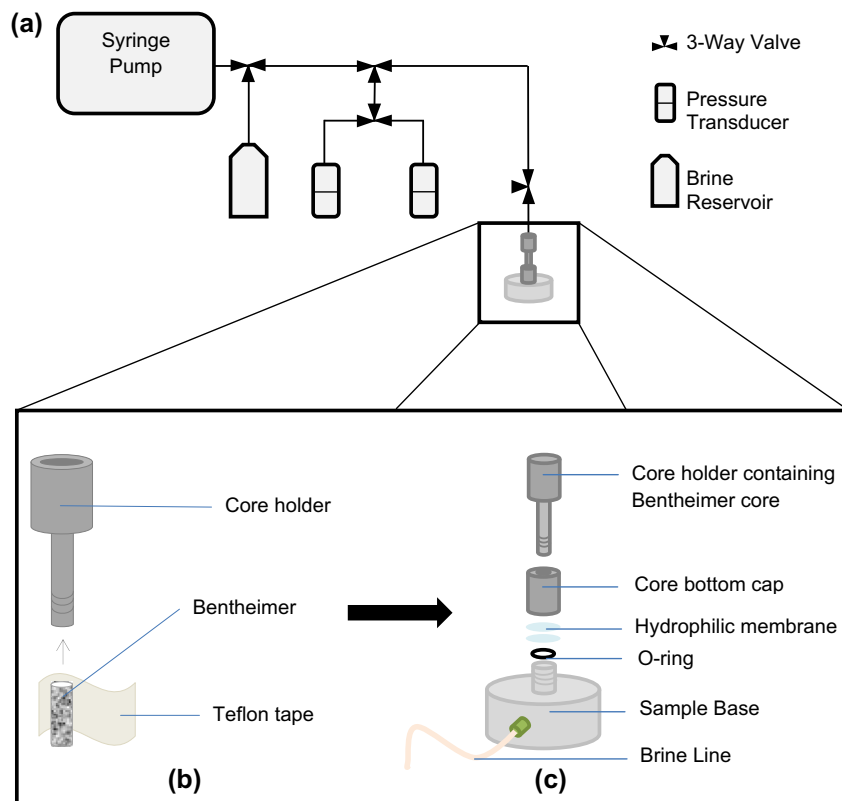
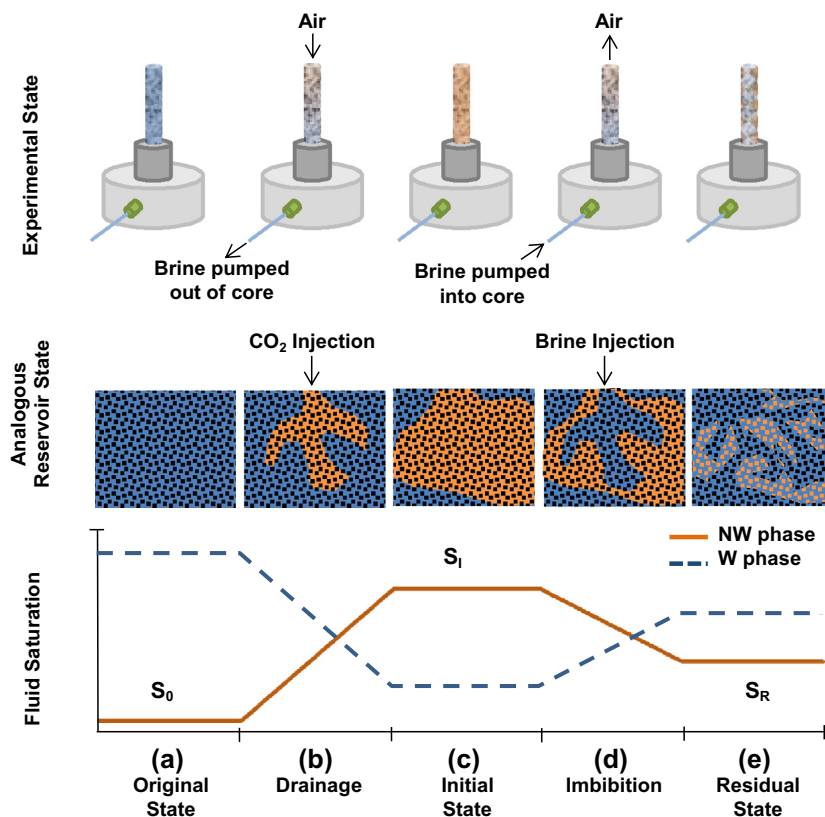


Fig. 2. Bentheimer sandstone NW trapping experiments: (a) experimental set-up schematic, (b) core holder preparation, and (c) sample assembly.



**Fig. 3.** Experimental process and analogy to reservoir CO<sub>2</sub> sequestration processes: (a) Original state,  $S_0$ : reservoir prior to CO<sub>2</sub> injection; (b) Drainage: reservoir during CO<sub>2</sub> injection; (c) Initial state,  $S_1$ : reservoir just after CO<sub>2</sub> injection; (d) Imbibition: reservoir during waterflood injection or natural groundwater flow; and (e) Residual state,  $S_R$ : final reservoir state after migration of mobile CO<sub>2</sub> plume and reinvasion of the pore space by wetting (W) phase.

determined by visual inspection and used for further analysis. For every data set, the upper and lower threshold values were consistently separated by 1000 grayscale values, so the kriging process is applied only to voxels with grayscale values in that range, out of the total grayscale range of 65,535 values.

In order to remove noise which manifested as falsely labeled NW phase blobs in the volume, a filter was applied using the commercial software Avizo<sup>®</sup> Fire which labeled all NW-labeled blobs less than a volume of 100 voxels as solid/W phase. 100 voxels corresponds to a volume of 100,000  $\mu\text{m}^3$  ( $10 \times 10^{-7}$  ml), equivalent to a cube with length of approximately 46  $\mu\text{m}$  per side, or a sphere of radius 29  $\mu\text{m}$ . This approach removed less than 1% of the NW phase.

At this point, Avizo<sup>®</sup> Fire was used to quantify the amount of non-wetting phase present in each volume, calculate blob volumes and numbers, determine a composite Euler number (i.e. a total summed Euler number for the entire volume), and create an iso-surface of the NW fluid within the core.

Due to the small sample sizes and the need to compare data from multiple rock cores, it was necessary to ensure that the data comprised a proper representative elementary volume (REV). Fig. 5a shows representative NW phase saturations as a function of cubical analytical volume for the three saturation states. There appears to be a plateau between subvolume sizes of approximately 250<sup>3</sup> and 350<sup>3</sup> voxels, followed by a consistent decrease in saturation as the subvolume approaches 550<sup>3</sup> voxels (the core diameter is approximately 750 pixels). The plateau suggests that sufficient size for a REV has been achieved, while the decreasing trend implies that regions near the core walls may have impeded flow of NW fluid during drainage. Therefore, in order to ensure that a REV had been achieved while removing potential wall flow issues

from analysis, cubes of 350  $\times$  350  $\times$  350 voxels were used for all quantitative analysis, corresponding to approximately 45 mm<sup>3</sup>. The size of the REV found here compares well with the study of Costanza-Robinson et al., who investigated REV sizes for a range of media types and grain sizes and found that the porosity REV ranged from 0.05 to 8 mm<sup>3</sup> and the saturation REV ranged up to a maximum of 51 mm<sup>3</sup> for images with voxel resolutions of 10.6–11.3  $\mu\text{m}$  [38]. As additional confirmation of this approach, Fig. 5b shows the Ca-saturation relationships as calculated from 350<sup>3</sup> voxel cubes and 550<sup>3</sup> voxel cubes. As shown, the general trend is reproduced regardless of which size subvolume is used.

### 2.1.3. Sintered glass bead column

Trapping experiments have also been performed on sintered glass bead columns with the same fluids, flow rates and experimental set-up to the Bentheimer experiments described above [34]. Sintered glass bead cores provide a model unconsolidated porous medium with significantly larger grain sizes than the sandstone, thus allowing for more accurate segmentation. Glass bead data was collected with the same X-ray CMT system as used for the Bentheimer experiments, but at a voxel size of approximately 13 microns. Segmentation and analysis were performed with Avizo<sup>®</sup> Fire; full details can be found in [34].

## 2.2. Loose packed glass bead and crushed tuff

The remaining data sets analyzed in this study were collected via synchrotron based X-ray microtomography [35,36]. In contrast to the trapping experiments described above, these data consist of multiple images taken throughout a series of imbibition and drainage cycle experiments. The glass bead cores were similar in size

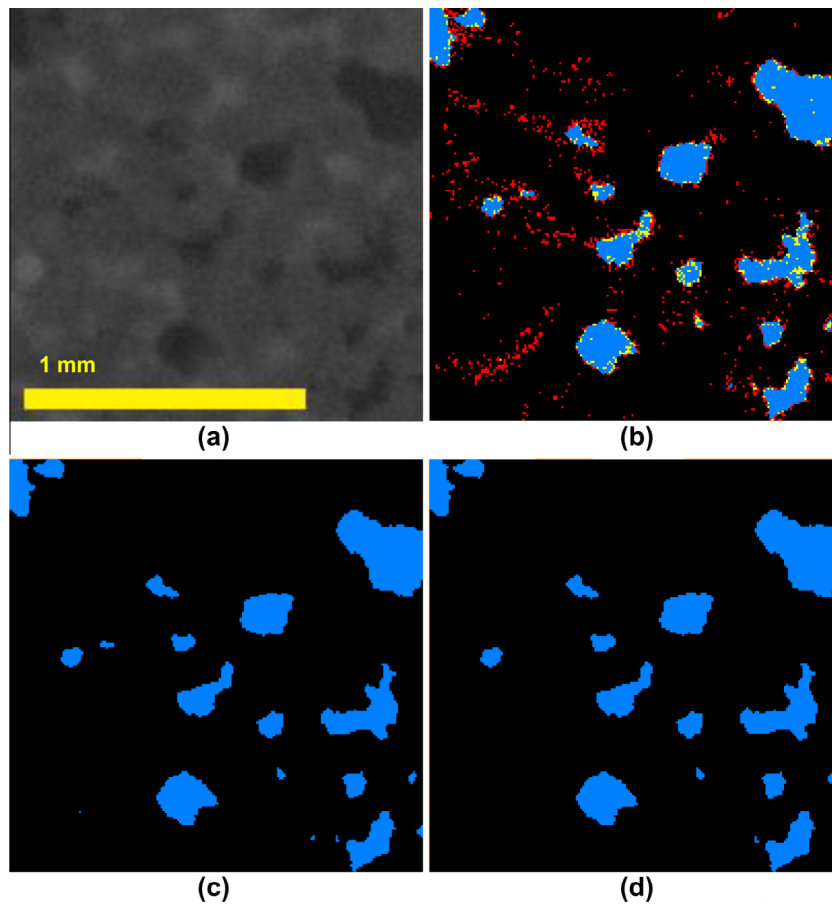


**Fig. 4.** Segmentation of the 3D Bentheimer data sets acquired by X-ray computed microtomography via the program 3DMA-Rock. A grayscale image (a) is labeled with an indicator Kriging algorithm (b) where the solid and the wetting phase are both labeled black, and the nonwetting fluid is labeled blue. The red label indicates voxels with grayscale values between the threshold limits which have been determined to be solid, and the yellow label indicate voxels with grayscale values between the threshold limits which have been determined to be NW fluid. Segmented image (c) shows the solid and the wetting phase in black and the nonwetting phase in blue. Final image (d) shows the result after the 100 voxel size exclusion filter has been applied.

and composition to the glass bead cores described above, although they were loosely packed (i.e. not sintered); full details can be found in [35]. Experiments were also conducted on similar sized columns of packed volcanic tuff, full details can be found in [36]. Glass bead and tuff data had a resolution of 17 and 16.8  $\mu\text{m}$ , respectively. For both data sets, a 3D majority filter with a kernel size of  $3 \times 3 \times 3$  was applied prior to quantification of connectivity and saturation; again, all analysis was performed using Avizo<sup>®</sup> Fire.

### 3. Theory

Topology is the study of *connectivity*, as opposed to shape; and one often studies the properties of an object that are invariant under deformations, such as bending and stretching, which change the object's shape but not its connectivity. The Euler number ( $\chi$ ) is a topological invariant which we use in this work to characterize the connectivity of the NW phase. For a 3D object, the Euler number is defined as

$$\chi = \beta_0 - \beta_1 + \beta_2$$

where  $\beta_0$  is the zeroth Betti number, referring to the number of distinct elements of fluid in the volume;  $\beta_1$  is the first Betti number, which refers to the number of "handles" or redundant loops present in the structure of each fluid component; and  $\beta_2$  is the second Betti number, indicating the number of enclosed voids in the fluid component. Values of the Betti numbers and Euler numbers for some simple shapes are shown in Fig. 6, adapted from Wildenschild and Sheppard [30].

In the context of NW fluid in porous media, features that would contribute to  $\beta_0$  include a small, isolated, bubble that occupies a single pore space, as well as a large, connected, multi-pore NW fluid element; both these examples have a  $\beta_0 = 1$ . In contrast, a single-pore isolated bubble has no contribution to  $\beta_1$ ; but a highly-branched multi-pore fluid element can have a relatively large contribution to  $\beta_1$ , depending on the number of redundant NW fluid-filled pore throats which connect the fluid bodies. Another method to describe  $\beta_1$  is to consider how many "cuts" one would need to make to disconnect an object; for example in Fig. 6e, it is possible to make a maximum of five cuts without creating two separate objects. Thus, in Fig. 6e, there are five redundant connections within the object; for an analogous fluid body within a porous medium, there would be five redundant pathways through which fluid could travel. In this study,  $\beta_2$  of the NW phase (air) is assumed to be zero since an element of W phase (water) or a solid particle cannot be completely suspended and surrounded by air. So, when interpreting Euler values presented in this work, the Euler number can be assumed to be simply:

$$\chi = \beta_0 - \beta_1$$

This is in agreement with topological analysis performed by Vogel [20]. From Fig. 6 we see that an object with more redundant connections (higher connectivity) has a more negative Euler number. The Euler numbers of all the connected pore spaces considered here are large and negative.

To allow comparison between different porous media, we define the *normalized Euler number* ( $\tilde{\chi}$ ) as the ratio between the

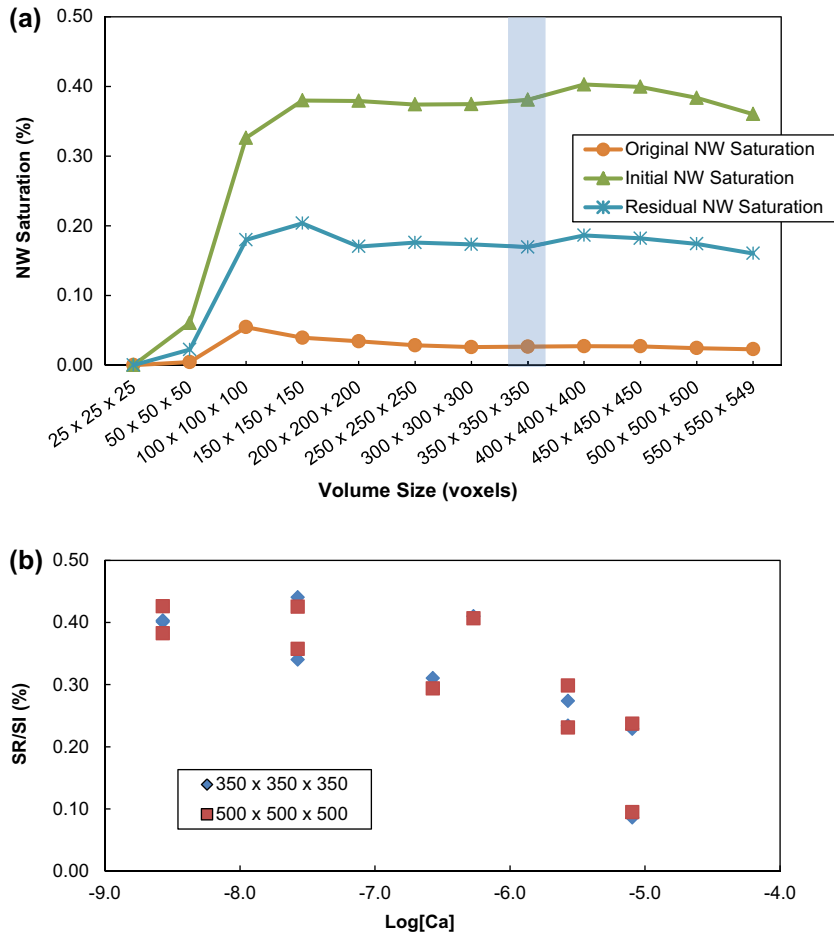


**Fig. 5.** Representative elementary volume (REV) analysis of cubic data sets from 3D X-ray microtomography image of Bentheimer sandstone. In (a) the nonwetting (NW) saturation is plotted as a function of data cube size for three different data sets: prior to drainage, “Original NW Saturation”; post-drainage, “Initial NW Saturation”; and post-imbibition, “Residual NW Saturation”. The data size selected for subsequent analysis,  $350 \times 350 \times 350$  voxels, is highlighted by the shaded area. In (b) residual NW saturation ( $S_R$ ) normalized by initial NW saturation ( $S_i$ ) is plotted as a function of Capillary number (Ca) for the of  $350^3$  and  $550^3$  voxel datasets of Bentheimer sandstone.

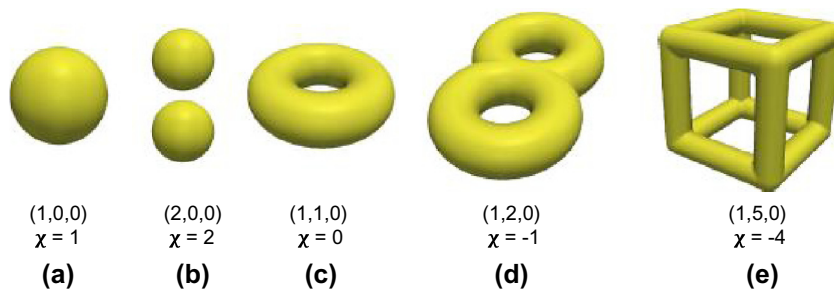


**Fig. 6.** Betti Numbers ( $\beta_0, \beta_1, \beta_2$ ) and Euler values ( $\chi$ ) for simple 3D solid objects: (a) Single sphere, (b) two disjoint spheres, (c) torus, (d) double torus, and (e) cubic frame.

NW phase Euler number ( $\chi$ ) and the Euler number of the sample at 100% NW phase ( $\chi_{100\% NW}$ ). Note that  $\chi_{100\% NW}$  is equal to the Euler number of the entire pore space and that since it is invariably a negative value, normalization changes the sign of  $\chi$ . Also, in addition to assuming  $\beta_2 = 0$  as above, we also assume that at partial saturation values, the NW phase does not contain any  $\beta_1$  features that are not present at 100% NW saturation; i.e. all NW phase loops encircle solid phase (or solid/W phase), as compared to a NW loop formed around pure W phase. This assumption results in the fact that a sample at 100% NW saturation has the most connected NW topology of any possible saturation state for that particular sample. Thus, as the normalized Euler number approaches 1.0 for a given porous medium, the system is approaching maximum

NW phase connectivity for that medium. Values of the normalized Euler number less than 0 indicate disconnected NW phase; more highly negative values indicate a larger number of disconnected, individual blobs of NW phase relative to the total connectivity for that specific media.

**4. Results**

*4.1. Connectivity-saturation relationships for various media*

The connectivity of NW fluid was investigated as a function of NW saturation for the four media types studied: Bentheimer

sandstone, sintered glass bead packs, loosely packed glass bead columns, and a pack of crushed tuff. Fig. 7a includes connectivity values for varying saturation levels throughout the drainage and imbibition processes the new trapping experiments in Bentheimer sandstone and sintered glass beads, and Fig. 7b shows connectivity values for the traditional drainage-imbibition scanning curve experiments in the loose glass bead pack and crushed tuff column. For all media types, the normalized Euler number increases as NW saturation increases, achieving a value of 1.0 at 100% NW saturation. For both glass bead data sets and the tuff data, this maximum connectivity value was determined from the dry scan of the single column used in experiments; for Bentheimer, the average of three dry scans from three different rock cores was used. Positive  $\hat{\chi}$  values indicate more highly connected NW phase, as shown by a cross-section of the NW phase in each volume in Fig. 8. For all systems,  $\hat{\chi}$  values cluster near 0 at low NW saturation, and some have negative values. Negative values imply the presence of disconnected NW blobs, as illustrated in Fig. 9. The transition from negative (dominantly disconnected) to positive (dominantly connected) NW fluid occurs below 50% NW saturation for the Bentheimer, and both glass bead cores; and above 50% NW saturation for the tuff core (Fig. 7). Note that the Euler number at 100% NW saturation ( $\chi_{100\% \text{ NW}}$ ) for the tuff pore space is an order of magnitude smaller than that of the sintered glass bead or Bentheimer samples (Table 2). Similarly, small subvolume size for the loose glass bead

pack (compared to the sintered bead column) results in a  $\chi_{100\% \text{ NW}}$  value about half that of the sintered glass bead column. The smaller  $\chi_{100\% \text{ NW}}$  may be partially responsible for forcing the disconnected normalized Euler values for the tuff and loose glass bead data sets to have larger negative values than their Bentheimer and sintered glass bead counterparts. The larger values for disconnected NW phase may also be a result of differences in the consolidation of the media (i.e. loose packed vs. sintered glass beads) or in how the experiments were performed (Pc-S curve experiments where brine is initially imbibed into a completely dry core, rather than draining a core saturated with wetting fluid).

The four porous media exhibit distinctly different *initial* normalized Euler numbers ( $\hat{\chi}_{init}$ ) as a function of NW saturation. At any given NW saturation, NW phase within Bentheimer sandstone displays higher connectivity than glass beads and tuff samples. Although the initial normalized Euler values for the sintered glass bead pack are clustered over a rather narrow range of NW saturation (approximately 80% to 95% NW phase), comparison of Fig. 7a and b show that both the sintered and loose glass bead pack show drainage values of approximately  $\hat{\chi}_{init} = 0.5$  at NW saturation of 90%. At low NW saturation, tuff samples exhibit relatively less well-connected NW phase (more negative initial normalized Euler values) than the Bentheimer or either glass bead pack, but at higher saturations (>~80%), the tuff and bead samples appear to converge.

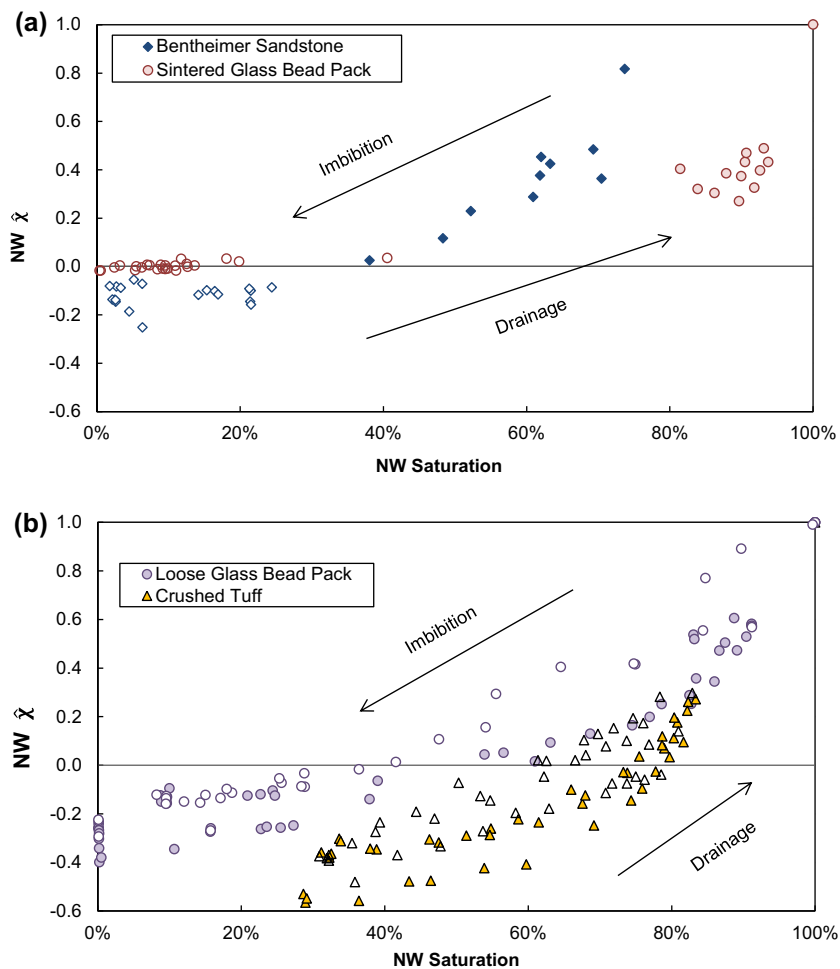


**Fig. 7.** Nonwetting (NW) phase connectivity ( $\hat{\chi}$ ) as a function of NW phase saturation for (a) Bentheimer sandstone, and sintered glass bead pack (trapping experiments); and (b) loose glass bead pack, and crushed tuff (drainage-imbibition scanning curve experiments). Drainage values are shown as solid symbols, imbibition values as hollow symbols.

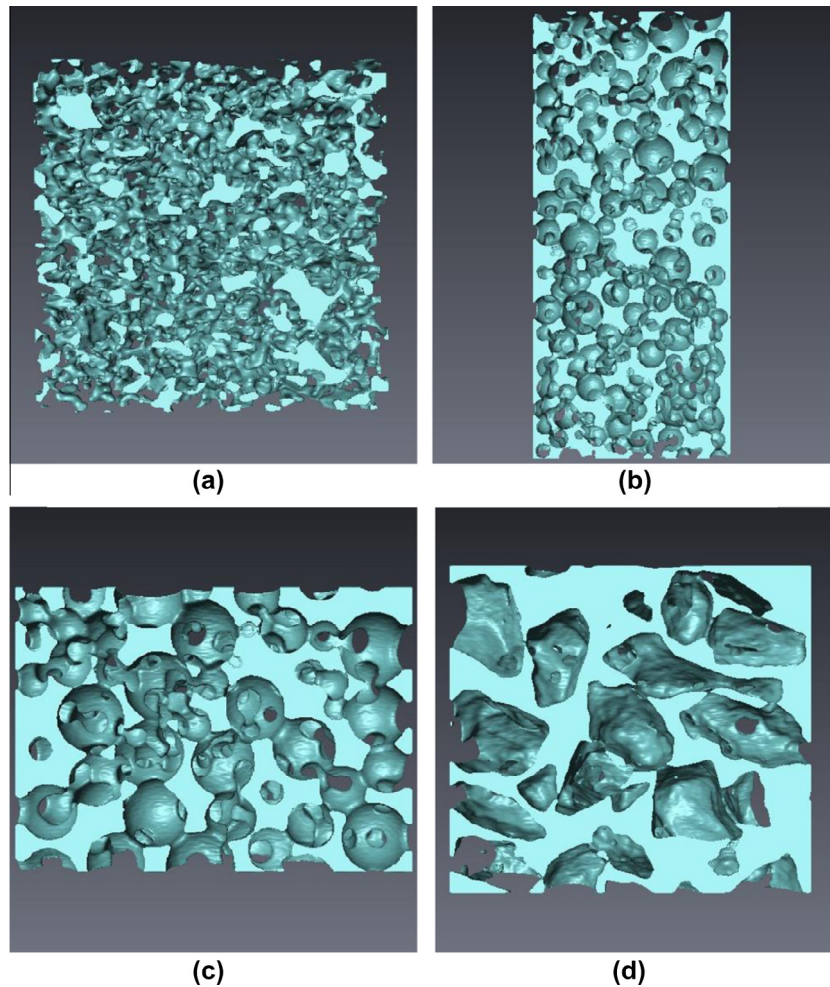


**Fig. 8.** Cross-sectional NW phase isosurfaces of: (a) Bentheimer sandstone (NW saturation = 63%,  $\hat{\chi} = 0.42$ ), (b) sintered glass bead pack (NW saturation = 90%,  $\hat{\chi} = 0.31$ ), (c) loose glass bead pack (NW saturation = 90%,  $\hat{\chi} = 0.53$ ), and (d) crushed tuff (NW saturation = 100%,  $\hat{\chi} = 1.00$ ).

#### 4.2. Influence of connectivity on NW trapping

Experiments were conducted in both Bentheimer sandstone and the sintered glass bead pack to explore the effects of connectivity on NW phase trapping; it was found that initial phase connectivity has a significant effect on residual NW capillary trapping for Bentheimer sandstone, but little or no effect on the glass bead system (Figs. 10 and 11).

NW capillary trapping ( $S_R/S_I$ ) decreases as a function of increasing Ca number in Bentheimer sandstone (Fig. 10). Notably different trapping values were identified for several experiments conducted at the same or similar capillary number values, as shown in Fig. 10, where these data points have been labeled with their initial normalized Euler number value (note that there are two data points overlaid at  $\log(\text{Ca}) = -8.6$ ). Data points with more well-connected initial NW phase (normalized Euler number values closer to 1.0) tend to correlate with significantly lower trapping values.

The Bentheimer sandstone exhibits an inverse relationship between residual trapping and normalized initial Euler number ( $R^2 = 0.78$ ) over the range of imbibition Ca investigated (i.e.  $\text{Ca} = 10^{-8.6} - 10^{-5.1}$ ). Conversely, the glass bead pack shows a weak inverse correlation ( $R^2 = 0.13$ ). This implies that initial phase connectivity has a significant effect on residual NW capillary trapping for Bentheimer sandstone, but minor to no effect on the glass bead system (Fig. 11).

#### 4.3. Repeatability of connectivity-saturation relationships

The drainage-imbibition experiments provide insight to the response of a porous medium to multiple scanning cycles. Saturation-connectivity relationships for the loose glass bead system and the crushed tuff are shown in Fig. 12; these plots distinguish between imbibition and drainage connectivity values. As shown, the saturation-connectivity relationships repeat over multiple drainage-imbibition cycles: for loose beads, three drainage-imbibition cycles were conducted; for the crushed tuff, four cycles. This suggests that the fluid configurations obtained during drainage and imbibition (at least via the main branches) are very similar and the measurements highly repeatable.

### 5. Discussion

Data from the four porous media analyzed demonstrate that while there are common characteristics among the saturation-connectivity relationships for the different media, there are also distinct differences (Fig. 7). The distinct  $\hat{\chi}_{init}$  vs. NW saturation trends shown indicate that it may be possible to select for desired connectivity that facilitate optimal residual trapping, by injecting NW fluid to a predetermined saturation.

NW phase topology plays a crucial role in determining NW phase capillary trapping for Bentheimer; however, there is no such trend for glass bead experiments (Figs. 10 and 11). Wardlaw

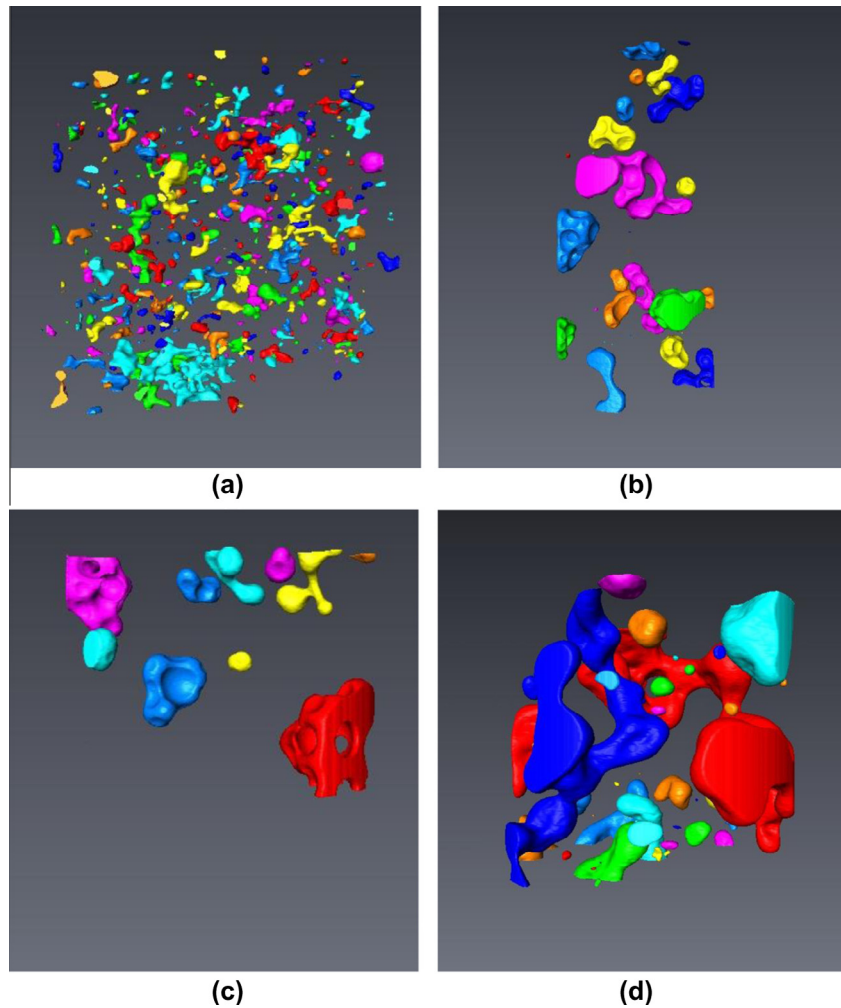


**Fig. 9.** Disconnected NW phase isosurfaces, with individual NW fluid blobs color-labeled of: (a) Bentheimer sandstone (NW saturation = 6%,  $\chi = -0.25$ ), (b) sintered glass bead pack (NW saturation = 11%,  $\chi = -0.12$ ), (c) loose glass bead pack (NW saturation = 9%,  $\chi = -0.16$ ), and (d) crushed tuff (NW saturation = 29%,  $\chi = -0.57$ ).

**Table 2**  
Maximum connectivity values.

Medium	$\chi_{100\% NW}$	Physical size of analyzed data (cm <sup>3</sup> )
Bentheimer sandstone	-1890	0.04
Sintered glass bead	-2190	0.51
Loose pack glass bead	-870	0.19
Crushed tuff	-190	0.18

and Yu [23] state that the influence of NW topology is more important for systems with uniform pore size and lower pore body-pore throat aspect ratios. However, Bentheimer sandstone generally has a larger average pore body-throat aspect ratio than the sintered glass bead pack used here; i.e. aspect ratio of 3.2 (standard deviation of 3.3) for Bentheimer, vs. 2.2 (standard deviation of 1.0) for sintered glass beads as calculated following the methods of Sheppard et al. [39]. This implies that our results disagree with those of [23]. This inconsistency may be due to differences in the media analyzed (e.g. larger pore and throat sizes in 2D micromodels vs. smaller pore and throat sizes in 3D columns) or a difference in flow regimes. More work needs to be done to determine why these differences in trapping responses exist for these two media, and to allow us to make predictions whether fluid topology will be an important variable for optimal trapping in other media.

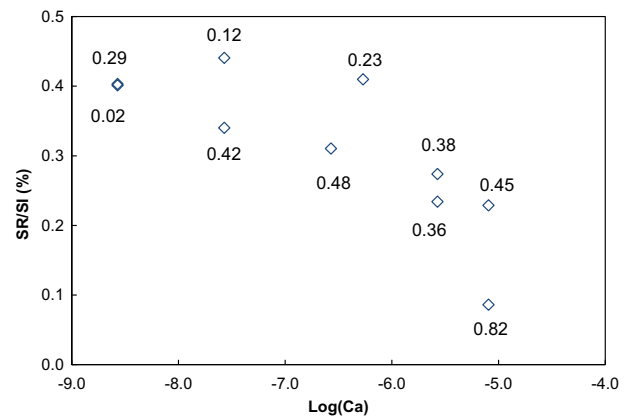


**Fig. 10.** The residual nonwetting (NW) saturation ( $S_R$ ) normalized by initial NW saturation ( $S_i$ ) plotted as a function of Capillary number ( $Ca$ ), with indicated NW normalized Euler number at initial saturation ( $NW\chi_{mit}$ ), for Bentheimer sandstone.

Many CO<sub>2</sub> sequestration scenarios will take place in formations with pore structures that are more similar to Bentheimer than glass beads or micromodels; therefore, it is likely that injection patterns and the subsequent initial NW phase topology within the medium will have an impact on the overall trapping of supercritical CO<sub>2</sub> within the subsurface. In order to optimize the capillary trapping mechanism, initial NW connectivity should be

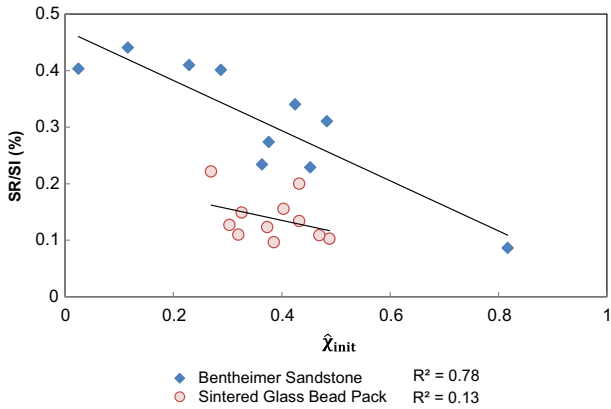


**Fig. 11.** The residual saturation ( $S_R$ ) normalized by initial saturation ( $S_I$ ) plotted as a function of normalized Euler number at initial saturation (after drainage) for Bentheimer sandstone and sintered glass bead pack.

considered and injection strategies should be designed to *minimize* initial NW phase connectivity.

The  $\hat{\chi}_{init}$  vs. NW saturation and the  $\hat{\chi}_{init}$  vs. trapping relationships are also in agreement with the initial-residual NW saturation relationships described by [13,14] and shown in Fig. 1, from [13]: residual saturation is positively correlated with initial saturation, but total trapping ( $S_R/S_I$ ) tends to decrease as initial saturation ranges from moderate (e.g. 50% NW phase) to high (e.g. > 90%). Injection to a moderate initial saturation would result in lower

NW connectivity, which in turn results in a larger fraction ( $S_R/S_I$ ) of  $CO_2$  that will be trapped via capillary trapping.

The connectivity-saturation repeatability data indicate that multiple injections will not significantly change the connectivity characteristics of the NW phase within the porous medium (Fig. 12). This implies that a WAG (water-alternating-gas) scheme, wherein multiple drainage-imbibition cycles are repeated continuously, would allow a system to maintain the original connectivity-saturation relationship. WAG injections have been suggested as a method to maximize capillary trapping of supercritical  $CO_2$ , and this has been investigated in modeling studies [40,41]. This work suggests that the mechanism by which WAG increases residual saturation is by decreasing the overall connectivity of the NW injection: a WAG type of injection pattern allows smaller volumes of  $CO_2$  to be injected per drainage process, thus reducing the local NW saturation in the medium, and consequently the local NW connectivity. This, in turn, would reduce the overall NW phase connectivity and facilitate capillary trapping, even for high-Ca imbibition processes (e.g. brine chase injection).

**6. Conclusions**

From a theoretical standpoint, this work provides 3D X-ray CMT based evidence to the concepts put forth by Wardlaw and Yu [23], namely:

- Higher initial state NW connectivity results in decreased residual NW capillary trapping in Bentheimer sandstone.

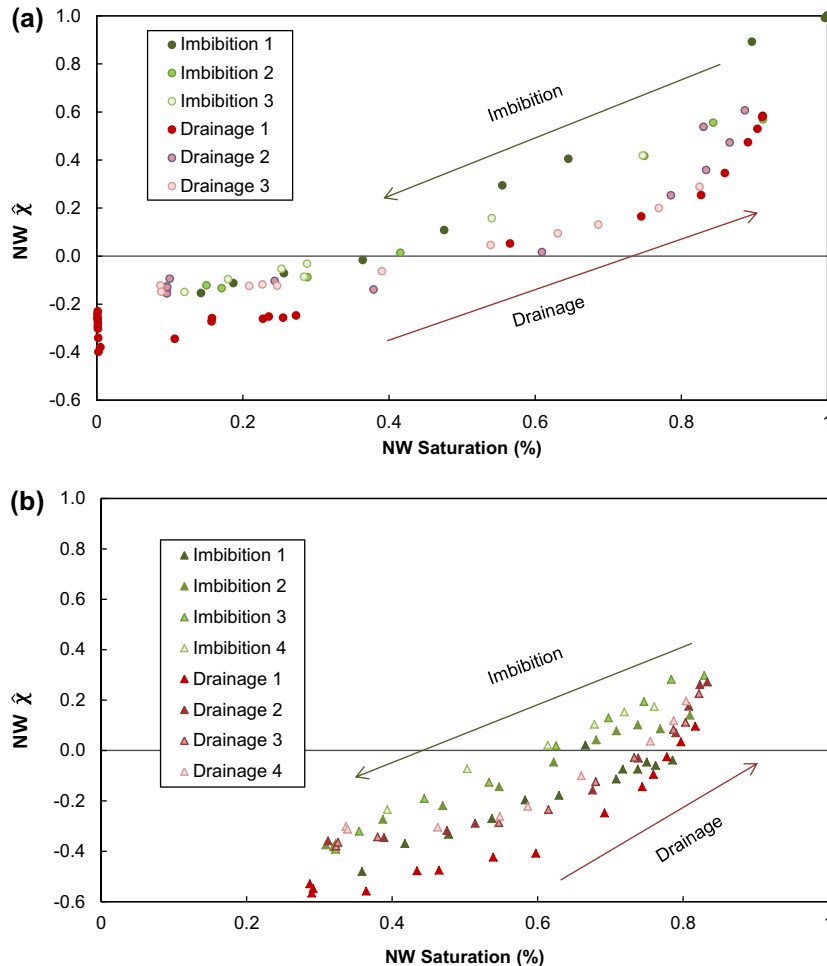


**Fig. 12.** Nonwetting (NW) normalized Euler number ( $\hat{\chi}$ ) as a function of NW saturation over multiple drainage-imbibition cycles for (a) loose glass bead pack, and (b) crushed tuff.

- The effect of NW topology (which we quantify with the normalized Euler number) is different for different types of media.

For application to geologic sequestration of supercritical CO<sub>2</sub>, this work demonstrates that:

- Capillary trapping is dependent on both (1) the drainage process which determines the initial NW connectivity, and (2) the Ca value of the imbibition process.
- Initial NW connectivity should be minimized to enhance CO<sub>2</sub> storage via capillary trapping (i.e. the number of redundant internal connections within the NW fluid phase component(s) after drainage should be minimized).
- It is possible to select for initial NW phase connectivity by injecting CO<sub>2</sub> to a pre-selected NW saturation.
- Multiple WAG-style injections will not disturb the original connectivity–saturation relationship of the medium, and will allow for multiple CO<sub>2</sub> injections to lower NW saturation values (and thus lower connectivity) rather than a single injection to a relatively high CO<sub>2</sub> saturation (and thus higher connectivity).
- A WAG injection pattern will likely enhance capillary trapping of CO<sub>2</sub> in the subsurface, even at high Ca imbibition (i.e. high brine or water chase flow rates).

Future work will be designed to explore which factors affect initial NW connectivity (i.e. drainage flow rate, fluid characteristics, and wettability impacts) in addition to initial NW saturation. More work is also necessary to determine which characteristics will dictate whether NW topology is important for a given medium.

## Acknowledgments

We gratefully acknowledge the support of the U.S. Department of Energy through the LANL/LDRD Program (#20100025DR) for this work; as well as the Department of Energy's Basic Energy Sciences, Geosciences Program via Grant number DE-FG02-11ER16277. The research of Adrian Sheppard is supported by an Australian Research Council Future Fellowship (FT100100470).

## References

- [1] IPCC. Climate change 1995: The science of climate change: Contribution of working group I to the second assessment report of the intergovernmental panel on climate change. Cambridge University Press; 1996.
- [2] Schrag DP. Preparing to capture carbon. *Science* 2007;315:812–3. <http://dx.doi.org/10.1126/science.1137632>.
- [3] IPCC. Ipc special report on carbon dioxide capture and storage; 2005.
- [4] Chatzis I, Morrow NR. Correlation of capillary number relationships for sandstone. *SPEJ Soc Pet Eng J (United States)* 1984;24(5):555–62.
- [5] Yadali Jamaloei B, Asghari K, Kharrat R. The investigation of suitability of different capillary number definitions for flow behavior characterization of surfactant-based chemical flooding in heavy oil reservoirs. *J Petrol Sci Eng* 2012;90–91:48–55. <http://dx.doi.org/10.1016/j.petrol.2012.04.020>.
- [6] Cense AW, Berg S. The viscous-capillary paradox in 2-phase flow in porous media. In: International symposium of the society of core analysts. Shell International Exploration & Production, Noordwijk, The Netherlands, 2009.
- [7] Suekane T, Zhou N, Hosokawa T, Matsumoto T. Direct observation of trapped gas bubbles by capillarity in sandy porous media. *Transp Porous Media* 2010;82:111–22. <http://dx.doi.org/10.1007/s11242-009-9439-5>.
- [8] Chatzis I, Kuntamukkula MS, Morrow NR. Effect of capillary number on the microstructure of residual oil in strongly water-wet sandstones. *SPE (Society of Petroleum Engineers) Reserv Eng (United States)* 1988;3(3):902–12.
- [9] Morrow NR, Chatzis I, Taber JT. Entrapment and mobilization of residual oil in bead packs. *SPE (Society of Petroleum Engineers) Reserv Eng (United States)* 1988;3(3):927–34.
- [10] Hughes RG, Blunt MJ. Pore scale modeling of rate effects in imbibition. *Transp Porous Media* 2000;40:295–322. <http://dx.doi.org/10.1023/A:1006629019153>.
- [11] Nguyen VH, Sheppard AP, Knackstedt MA, Val Pinczewski W. The effect of displacement rate on imbibition relative permeability and residual saturation. *J Petrol Sci Eng* 2006;52:54–70. <http://dx.doi.org/10.1016/j.petrol.2006.03.020>.
- [12] Ding M, Kantzas A. Capillary number correlations for gas–liquid systems. Calgary, Canada: Society of Petroleum Engineers; 2007.
- [13] Al Mansoori SK, Itsekiri E, Iglauer S, Pentland CH, Bijeljic B, Blunt MJ. Measurements of non-wetting phase trapping applied to carbon dioxide storage. *Int J Greenhouse Gas Control* 2010;4:283–8. <http://dx.doi.org/10.1016/j.ijggc.2009.09.013>.
- [14] Land C. Calculation of imbibition relative permeability for two and three-phase flow from rock properties. *Old SPE J* 1968;8:149–56.
- [15] Wardlaw NC. Mechanisms of nonwetting phase trapping during imbibition at slow rates. *J Colloid Interface Sci.* 1986;109:473–86.
- [16] Sok RM, Knackstedt MA, Sheppard AP, Pinczewski W, Lindquist W, Venkatarangan A, et al. Direct and stochastic generation of network models from tomographic images; effect of topology on residual saturations. *Transp Porous Media* 2002;46:345–71.
- [17] Vogel HJ. Topological characterization of porous media. *Morphol Condens Matter* 2002;75–92.
- [18] Arns JY, Robins V, Sheppard AP, Sok RM, Pinczewski W, Knackstedt MA. Effect of network topology on relative permeability. *Transp Porous Media* 2004;55:21–46.
- [19] Mahmud WM, Arns JY, Sheppard A, Knackstedt MA, Pinczewski WV. Effect of network topology on two-phase imbibition relative permeability. *Transp Porous Media* 2007;66:481–93.
- [20] Vogel HJ, Weller U, Schlüter S. Quantification of soil structure based on minkowski functions. *Comput Geosci* 2010;36:1236–45.
- [21] Chatzis I, Morrow N, Lim H. Magnitude and detailed structure of residual oil saturation. *Old SPE J* 1983;23:311–26.
- [22] Al-Raoush RI, Willson CS. A pore-scale investigation of a multiphase porous media system. *J Contam Hydrol* 2005;77:67–89. <http://dx.doi.org/10.1016/j.jconhyd.2004.12.001>.
- [23] Wardlaw NC, Yu L. Fluid topology, pore size and aspect ratio during imbibition. *Transp Porous Media* 1988;3:17–34. <http://dx.doi.org/10.1007/bf00222684>.
- [24] Youssef S, Bauer D, Bekri S, Rosenberg E, Vizika-kavvadias O. 3d in situ fluid distribution imaging at the pore scale as a new tool for multiphase flow studies. In: SPE annual technical conference and exhibition; 2010.
- [25] Setiawan A, Nomura H, Suekane T. Microtomography of imbibition phenomena and trapping mechanism. *Transp Porous Media* 2012;92:243–57. <http://dx.doi.org/10.1007/s11242-011-9899-2>.
- [26] Wildenschild D, Vaz CMP, Rivers ML, Rikard D, Christensen BSB. Using x-ray computed tomography in hydrology: systems, resolutions, and limitations. *J Hydrol* 2002;267:285–97. [http://dx.doi.org/10.1016/S0022-1694\(02\)00157-9](http://dx.doi.org/10.1016/S0022-1694(02)00157-9).
- [27] Silin D, Tomutsa L, Benson S, Patzek T. Microtomography and pore-scale modeling of two-phase fluid distribution. *Transp Porous Media* 2011;86:495–515. <http://dx.doi.org/10.1007/s11242-010-9636-2>.
- [28] Ketcham RA, Carlson WD. Acquisition, optimization and interpretation of x-ray computed tomographic imagery: applications to the geosciences. *Comput amp Geosci* 2001;27:381–400. [http://dx.doi.org/10.1016/S0098-3004\(00\)00116-3](http://dx.doi.org/10.1016/S0098-3004(00)00116-3).
- [29] Blunt MJ, Dong H, Garbi O, Iglauer S, Mostaghimi P, et al. Pore-scale imaging and modelling. *Adv. Water Resour.* 2012. <http://dx.doi.org/10.1016/j.advwatres.2012.03.003>.
- [30] Wildenschild D, Sheppard AP. X-ray imaging and analysis techniques for quantifying pore-scale structure and processes in subsurface porous medium systems. *Adv Water Resour* 2012.
- [31] Lehman P, Wyss P, Flisch A, Lehmann E, Vontobel P, Krafczyk M, et al. Tomographical imaging and mathematical description of porous media used for the prediction of fluid distribution. *Vadose Zone J.* 2006;5:80–97. <http://dx.doi.org/10.2136/vzj2004.0177>.
- [32] Hilpert M, Glantz R, Miller CT. Calibration of a pore-network model by a pore-morphological analysis. *Transp Porous Med* 2003;51:267–85.
- [33] Polak S, Cinar Y, Holt T, Torsæter O. An experimental investigation of the balance between capillary, viscous, and gravitational forces during CO<sub>2</sub> injection into saline aquifers. *Energy Procedia* 2011;4:4395–402. <http://dx.doi.org/10.1016/j.egypro.2011.02.392>.
- [34] Harper EJ. Optimization of capillary trapping for CO<sub>2</sub> sequestration in saline aquifers. Corvallis, Oregon: Oregon State University; 2012.
- [35] Culligan KA, Wildenschild D, Christensen BS, Gray WG, Rivers ML, Tompson AF. Interfacial area measurements for unsaturated flow through a porous medium. *Water Resour Res* 2004;40:W12413.
- [36] Joekar-Niasar V, Doster F, Armstrong RT, Wildenschild D, Celia MA. Trapping and hysteresis in two-phase flow in porous media: a pore-network study. *Water Resour Res* (submitted for publication).
- [37] Oh W, Lindquist B. Image thresholding by indicator kriging. *IEEE Trans Pattern Anal Mach Intell* 1999;21:590–602.
- [38] Costanza-Robinson MS, Estabrook BD, Fouhey DF. Representative elementary volume estimation for porosity, moisture saturation, and air–water interfacial areas in unsaturated porous media: data quality implications. *Water Resour Res* 2011;47:W07513. <http://dx.doi.org/10.1029/2010wr009655>.
- [39] Sheppard A, Sok R, Averdunk H, Robins V, Ghaus A. Analysis of rock microstructure using high-resolution X-ray tomography. In: Proceedings of the International Symposium of the Society of Core Analysts 2006.
- [40] Juanes R, Spiteri EJ, Orr Jr FM, Blunt MJ. Impact of relative permeability hysteresis on geological CO<sub>2</sub> storage. *Water Resour Res* 2006;42:W12418. <http://dx.doi.org/10.1029/2005wr004806>.
- [41] Jessen K, Kovscek AR, Orr Jr FM. Increasing CO<sub>2</sub> storage in oil recovery. *Energy Convers Manage* 2005;46:293–311. <http://dx.doi.org/10.1016/j.enconman.2004.02.019>.